Modeling of the transport phenomena in GMAW using argon–helium mixtures. Part I – The arc

Z.H. Rao [a,b], J. Hu [c], S.M. Liao [a], H.L. Tsai [b,*]

[a] School of Energy Science and Engineering, Central South University, Changsha 410083, China
[b] Department of Mechanical and Aerospace Engineering, Missouri University of Science and Technology, Rolla, MO 65409, USA
[c] Department of Mechanical Engineering, University of Bridgeport, Bridgeport, CT 06604, USA

ABSTRACT

This article presents a numerical investigation on the transient transport phenomena in the arc which include the arc plasma generation and interactions with moving droplets and workpiece for pure argon and three argon–helium mixtures (75% Ar + 25% He, 50% Ar + 50% He, and 25% Ar + 75% He) during the gas metal arc welding (GMAW) process. The results indicate that the arcs in various shielding gases behave very differently due to the significant differences in thermophysical properties, including the ionization potential and the electrical conductivity, thermal conductivity, specific heat, and viscosity at high temperatures. For the same welding power input, it was found the increase of helium content in the mixtures results in (1) the change of plasma arc shape from bell-like to cone-like and (2) the change of arc pressure distribution along the workpiece surface from Gaussian-like to flat-top with decreasing peak value. Detailed explanations to the physics of the very complex but interesting transport phenomena are given.

© 2010 Elsevier Ltd. All rights reserved.

1. Introduction

The shielding gas composition is a critical parameter in the GMAW process. The primary function of shielding gas in GMAW is to provide a protective environment for the molten metal from being oxidized. It also plays an important role in affecting arc characteristics, mode of metal transfer, weld pool dynamic, weld bead profile and weld penetration [1] which, in turn, determines the efficiency, quality and overall performance of the welding operation. The selection of shielding gas for achieving better welding performance has been studied extensively, although mainly by experiments [2–6]. An increasing range of shielding gas is available for arc welding, which varies from pure gas to binary, ternary or even quaternary mixtures based on argon, helium, carbon dioxide, hydrogen and oxygen.

Argon and helium are the most common shielding gases used in GMAW. Both argon and helium are inert gases which cannot react with the molten weld pool. However, they differ in physical properties, including density, thermal conductivity, electrical conductivity, and ionization potential, and these differences can significantly influence the characteristics of arc plasma and molten metal in GMAW. The major difference is that helium has a higher ionization potential, 24.58 V as compared to 15.755 V for argon. For this reason, a much higher arc voltage is required to ionize helium and thus produces a

higher arc power density at the same current level. In contrast, argon requires a lower arc voltage for ionization, which facilitates a better arc starting and arc stability. Helium is a good conductor of thermal energy with higher thermal conductivity than argon. However, helium is more expensive than argon. Owing to the abovementioned features and characteristics, argon is often mixed with various percentages of helium to take the advantages of each gas.

To obtain satisfactory weld quality, it is essential to understand the role that shielding gas plays in heat transfer and fluid flow in the plasma arc of GMAW. Although experimental observations can provide some invaluable information, it is difficult to accurately measure arc parameters and reveal the underlying mechanisms during the GMAW process due to the extreme high temperature and high velocity. Therefore, numerical modeling has been broadly employed. In recent years, a number of articles have been published for modeling the transport phenomena of arc plasma during the GMAW process [7–14]. Modeling a GMAW process includes the following three events: (1) the generation and evolution of arc plasma, (2) the dynamic process of droplet formation, detachment, transfer and impingement onto the weld pool, and (3) the dynamics of weld pool and the formation of weld bead. Apparently, arc plasma interacts in a transient manner with the droplet and weld pool during the GMAW process. Due to the complexity of the welding process, most of the existing models deal with only one or two of these events while simplifying the rest. Recently, Hu and Tsai [15,16] developed a real unified model employing the volume of fluid (VOF) technique and the continuum formulation to simulate the entire GMAW process including all the

* Corresponding author. Tel.: +1 573 341 4945; fax: +1 573 341 4607.
E-mail address: tsai@mst.edu (H.L. Tsai).

Nomenclature

A_v	constant, defined in Eq. (19)
B_θ	self-induced azimuthal magnetic field
c	specific heat
C	coefficient, defined in Eq. (11)
c_1	permeability coefficient, defined in Eq. (10)
d	dendrite arm spacing
e	electronic charge
F	volume of fluid function
f	mass fraction
g	volume fraction or gravitational acceleration
h	enthalpy
H	latent heat of fusion
H_{ev}	latent heat of vaporization
I	welding current
J_a	anode current density
J_r	radial current density
J_z	axial current density
k	thermal conductivity
K	permeability, defined in Eq. (10)
k_b	Stefan–Boltzmann constant
k_{eff}	effective thermal conductivity at arc–metal interface
$\vec{n}$	vector normal to the local free surface
p	pressure
P_{atm}	atmospheric pressure
p_s	surface tension pressure
Q	shielding gas flow rate
q_{ev}	evaporation mass rate of metal vapor
r–z	cylindrical coordinate system
R	gas constant
R_n	internal radius of the shielding gas nozzle
R_w	radius of the electrode
$\vec{s}$	vector tangential to the local free surface
S_a	anode sheath energy heat flux for the metal
S_{ap}	anode sheath energy heat flux for the arc plasma
S_c	cathode sheath energy heat flux for the metal
S_{cp}	cathode sheath energy heat flux for the arc plasma
S_R	radiation heat loss

t	time
T	temperature
T_{arc}	arc plasma temperature close to the anode and cathode
T_a, T_c	anode, cathode surface temperature
T_l	liquidus temperature
T_s	solidus temperature
T_∞	ambient temperature
u	velocity in r-direction
v	velocity in z-direction
$\mathbf{V}$	velocity vector
$\mathbf{V}_r$	relative velocity vector $(V_l - V_s)$
V_w	wire feed rate
W	melt evaporation rate

Greek symbols

β_T	thermal expansion coefficient
γ	surface tension coefficient
$\partial\gamma/\partial T$	surface tension temperature gradient
ϵ	surface radiation emissivity
κ	free surface curvature
μ_l	dynamic viscosity
μ_0	magnetic permeability
ϕ	electric potential
ϕ_w	work function of the anode material
σ_e	electrical conductivity
ρ	density
τ_{ps}	plasma shear stress
τ_{Ms}	Marangoni shear stress
δ	length of the anode or cathode sheath
Δt	time interval

Subscripts

0	initial value
l	liquid phase
r	relative to solid phase velocity
s	solid phase
w	wire

aforementioned three events. In their study, however, only pure argon was considered as the shielding gas, and the effects of shielding gas composition were not included. It is expected that the addition of helium to argon will lead to significant changes in the structure and characteristics of the plasma arc that affects the metal transfer, weld bead formation and ultimately the weld quality. Up to date, very few models have been developed to study the effect of shielding gas composition on arc plasma in GMAW, especially for helium or argon–helium mixtures. Haidar and Lowke [17] numerically studied the effect of carbon dioxide in shielding gas on arc plasma and thus on the metal droplet formation. In their model, the droplet was ignored in the calculation after its detachment, the workpiece was treated as a flat plate, and the effects of shielding gas on metal transfer and weld pool were not considered. Jönsson et al. [18] developed a model to compare the argon arc and the helium arc in GMAW at a variety of current levels. In their model, however, the time-dependent behavior, periodic droplet formation, detachment and transfer toward the workpiece were all omitted, and the electrode tip and weld pool surface were assumed to be flat. In reality, the profile of the electrode tip changes rapidly and the surface of the weld pool is highly deformable during the GMA welding process. During the droplet transfer through the arc plasma and impinging onto the weld pool, the flow of arc plasma is dramatically distorted which, in turn, changes the transient distributions of temperature, velocity and current of the arc

plasma. Therefore, the effect of shielding gas with different argon–helium mixtures on arc plasma in GMAW has not been thoroughly understood yet.

It should be pointed out that the presence of metal vapor in the arc can change the thermophysical properties of the arc plasma [19–21] and, hence, the behaviors of the GMAW process [22,23]. It was shown that even a small amount of metal vapor increases the electrical conductivity of arc plasma at low temperatures (especially for helium gas) [19–21] with the result of better arc stability, and the radiative emission coefficient increases with increasing the mixing ratio of iron vapor [21]. Haidar [22] and Schnick et al. [23] studied the argon–iron arc in GMAW and found that the metal vapor emanating from electrode droplets decreases the arc temperature near the axis due to the dynamic effects [22] and the strong radiative emission from the iron vapor [23], which lead to the decrease in heat flux density and current density at the workpiece and thus a shallower weld pool. However, the integration of the metal vapor's effects into the model will greatly increase its complexity, which makes it difficult to identify the nature of the shielding gas in GMAW. In order to obtain the intrinsic characteristics in the arc and metal for various shielding gases, therefore, the effects of metal vapor are omitted in this study.

In this work, a transient unified model is applied to simulate the GMAW process with different shielding gases at a constant energy input including the arc, the metal and their interaction. The

emphasis is placed on the globular metal transfer in this study, thus a relatively low electric power is employed. The effects of shielding gas composition, including pure argon and argon–helium mixtures with various molar percentages of argon content (75% Ar, 50% Ar and 25% Ar), on the GMAW process are investigated in terms of (1) the characteristics of plasma arc, (2) the droplet formation, detachment, transfer and impingement onto the weld pool, and (3) the weld bead penetration and profile. This paper focuses on presenting the results of arc plasma, while a second accompany paper will discuss the transport phenomena in the metal region consisting of the electrode, droplet and workpiece. This study provides a better understanding of the role of shielding gas and gains the essential knowledge needed for the selection of shielding gas to achieve the optimum GMAW process.

2. Mathematical formulation

2.1. Governing equations

Fig. 1 is a schematic sketch of a stationary axisymmetric GMAW system. In this system, an electric current is supplied to the electrode through the contact tube at the top of the computational domain. A plasma arc is struck between the electrode and the workpiece. The electrode is continuously fed downward and then melted at the tip by the high temperature arc. Droplets are formed at the molten electrode tip, grow, and are then detached and transferred to the workpiece. A weld pool is formed at the workpiece by the continuous impingement of the droplets and the dynamic interaction with the high temperature and high pressure arc plasma. Inert shielding gas is provided through the shielding gas nozzle to prevent the molten metal from oxidation.

The calculation domain in Fig. 1 is divided into two regions: the arc region and the metal region. The metal region includes the electrode, the workpiece, and the detached droplets. In this model, the arc region and the metal region are calculated separately and coupled through the special boundary conditions at the metal–plasma interfaces [24,25]. The differential equations governing the arc and the metal can be put into a single set and are given below [26]:

Mass continuity

$$\frac{\partial}{\partial t}(\rho) + \nabla \cdot (\rho V) = 0. \tag{1}$$

Fig. 1. A schematic representation of a GMAW system including the electrode, the arc and the weld pool (not to scale).

Momentum

$$\frac{\partial}{\partial t}(\rho u) + \nabla \cdot (\rho V u) = \nabla \cdot \left(\mu_l \frac{\rho}{\rho_l} \nabla u\right) - \frac{\partial p}{\partial r} - \frac{\mu_l}{K} \frac{\rho}{\rho_l}(u - u_s)$$
$$- \frac{C\rho^2}{K^{1/2}\rho_l}|u - u_s|(u - u_s)$$
$$- \nabla \cdot (\rho f_s f_l V_r u_r) - J_z \times B_\theta \tag{2}$$

$$\frac{\partial}{\partial t}(\rho v) + \nabla \cdot (\rho V v) = \nabla \cdot \left(\mu_l \frac{\rho}{\rho_l} \nabla v\right) - \frac{\partial p}{\partial z} - \frac{\mu_l}{K} \frac{\rho}{\rho_l}(v - v_s)$$
$$- \frac{C\rho^2}{K^{1/2}\rho_l}|v - v_s|(v - v_s)$$
$$- \nabla \cdot (\rho f_s f_l V_r v_r) + \rho g \beta_T (T - T_0) + J_r \times B_\theta. \tag{3}$$

Energy

$$\frac{\partial}{\partial t}(\rho h) + \nabla \cdot (\rho V h) = \nabla \cdot \left(\frac{k}{c_s} \nabla h\right) + \nabla \cdot \left(\frac{k}{c_s} \nabla (h_s - h)\right)$$
$$- \nabla \cdot (\rho(V - V_s)(h_l - h))$$
$$- \Delta H \frac{\partial f_l}{\partial t} + \frac{J_r^2 + J_z^2}{\sigma_e} - S_R + \frac{5k_b}{2e}\left(\frac{J_r}{c_s}\frac{\partial h}{\partial r} + \frac{J_z}{c_s}\frac{\partial h}{\partial z}\right). \tag{4}$$

Current continuity

$$\nabla^2 \phi = \frac{1}{r}\frac{\partial}{\partial r}\left(r\frac{\partial \phi}{\partial r}\right) + \frac{\partial^2 \phi}{\partial z^2} = 0. \tag{5}$$

Ohm's law

$$J_r = -\sigma_e \frac{\partial \phi}{\partial r}, \quad J_z = -\sigma_e \frac{\partial \phi}{\partial z}. \tag{6}$$

Maxwell's equation

$$B_\theta = \frac{\mu_0}{r}\int_0^r J_z r \, dr. \tag{7}$$

The above equations are used to determine the basic physical parameters describing the arc plasma and metal region, including the pressure p, radial and axial velocities u and v, temperature T, electrical potential ϕ, radial and axial current densities J_r and J_z, and self-induced azimuthal magnetic field B_θ. The input material properties required for arc plasma, solid and liquid metal include density ρ, viscosity μ, specific heat c, thermal conductivity k, electrical conductivity σ_e, permeability function K, enthalpy h and inertial coefficient C. Note the effect of metal vapor on plasma properties is omitted in the present study. The plasma is assumed to be in local thermodynamic equilibrium (LTE) [25] and optically thin, thus the radiation may be modeled in an approximate manner by defining a radiation heat loss per unit volume S_R in Eq. (4) [25,27]. In Eq. (2), $\boldsymbol{V}_r = \boldsymbol{V}_l - \boldsymbol{V}_s$ is the relative velocity vector between the liquid phase and the solid phase in the mushy zone, where the solid phase velocity is assumed to be zero due to a relatively small weld pool (as compared to, for example, a casting), concentrated arc heat, and rapid solidification of the weld pool after the arc is turned off. A more detailed description of the assumptions and physical meanings for these equations is presented by Hu and Tsai [15], so it will not be repeated here.

In Eqs. (1)–(4), the continuum density, specific heat, thermal conductivity, solid mass fraction, liquid mass fraction, velocity, and enthalpy are defined as follows:
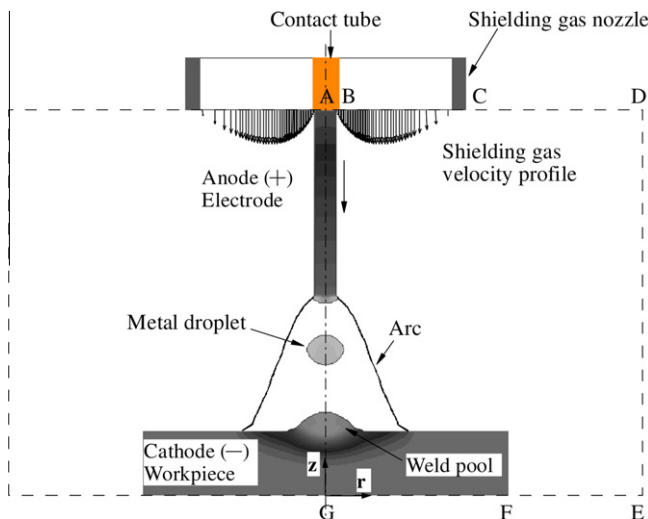
$$\rho = g_s\rho_s + g_l\rho_l, \quad c = f_sc_s + f_lc_l, \quad k = g_sk_s + g_lk_l,$$
$$f_s = \frac{g_s\rho_s}{\rho}, \quad f_l = \frac{g_l\rho_l}{\rho},$$
$$\boldsymbol{V} = f_s\boldsymbol{V}_s + f_l\boldsymbol{V}_l, \quad h = h_sf_s + h_lf_l. \tag{8}$$

Assuming constant phase specific heats, the phase enthalpy for the solid and liquid can be expressed as

$$h_s = c_sT, \quad h_l = c_lT + (c_s - c_l)T_s + H. \tag{9}$$

where H is the latent heat of fusion for the alloy.

The assumption of permeability function in the mushy zone requires consideration of the growth morphology specific to the alloy under study. In the present study, the permeability function analogous to fluid flow in porous media is assumed, employing the Carman–Kozeny equation [28,29]

$$K = \frac{g_l^3}{c_1(1 - g_l)^2}, \quad c_1 = \frac{180}{d^2}, \tag{10}$$

where d is proportional to the dendrite dimension, which is assumed to be a constant and is on the order of 10^{-2} cm. The inertial coefficient, C, can be calculated from [30]

$$C = 0.13g_l^{-3/2}. \tag{11}$$

2.2. Tracking of solid–liquid interface

The solid/liquid phase-change boundary is handled by the continuum model [26]. The third, fourth, and fifth terms on the right-hand-side of Eqs. (2) and (3) vanish at the solid phase because $u = u_s = v = v_s = 0$ and $f_l = 0$. For the liquid region, since K goes to infinity due to $g_l = 1$ in Eq. (7) and $f_s = 0$, all the aforementioned terms also vanish. These terms are only valid in the mushy zone, where $0 < f_l < 1$ and $0 < f_s < 1$. Therefore, there is no need to explicitly track the phase-change boundaries, and the liquid region, mushy zone, and solid region are all calculated by the same Eqs. (2) and (3). During the fusion and solidification processes, the latent heat is absorbed or released in the mushy zone, which is handled through the use of enthalpy defined in Eq. (9).

2.3. Tracking of free surfaces

The algorithm of volume of fluid (VOF) is used to track the moving free surface [31]. The fluid configuration is defined by a volume of fluid function, $F(r, z, t)$, which tracks the location of the free surface. This function represents the volume of fluid per unit volume and satisfies the following conservation equation:

$$\frac{dF}{dt} = \frac{\partial F}{\partial t} + (\boldsymbol{V} \cdot \nabla)F = 0. \tag{12}$$

When averaged over the cells of a computing mesh, the average value of F in a cell is equal to the fractional volume of the cell occupied by the metal. A unit value of F corresponds to a cell full of metal, whereas a zero value indicates the cell contains no metal. Cells with F values between zero and one are partially filled with metal.

2.4. Forces at the local free surface

The molten part of the metal is subjected to body forces such as gravity and electromagnetic force. It is also subjected to surface forces including the surface tension due to surface curvature, the Marangoni shear stress due to temperature difference, the arc plasma shear stress, and the arc pressure.

For cells containing a free surface, surface tension pressure normal to the free surface can be expressed as [32]

$$p_s = \gamma\kappa, \tag{13}$$

where γ is the surface tension coefficient and κ is the free surface curvature given by

$$\kappa = -\left[\nabla \cdot \left(\frac{\vec{n}}{|\vec{n}|}\right)\right] = \frac{1}{|\vec{n}|}\left[\left(\frac{\vec{n}}{|\vec{n}|} \cdot \nabla\right)|\vec{n}| - (\nabla \cdot \vec{n})\right], \tag{14}$$

where $\vec{n}$ is a vector normal to the local free surface which equals the gradient of the VOF function

$$\vec{n} = \nabla F. \tag{15}$$

The temperature-dependent Marangoni shear stress at the free surface in a direction tangential to the local free surface is given by Fan and Kovacevic [33]

$$\tau_{Ms} = \frac{\partial\gamma}{\partial T}\frac{\partial T}{\partial \vec{s}}, \tag{16}$$

where $\vec{s}$ is a vector tangential to the local free surface.

The arc plasma shear stress is calculated at the free surface from the velocities of the arc plasma cells immediately next to the metal cells.

$$\tau_{ps} = \mu\frac{\partial\boldsymbol{V}}{\partial\vec{s}}, \tag{17}$$

where μ is the viscosity of the arc plasma.

The arc pressure at the metal surface is obtained from the computational result in the arc region. The surface forces are included by adding source terms to the momentum equations according to the CSF (continuum surface force) model [32,34]. Using F of the VOF function as the characteristic function, surface tension pressure, Marangoni shear stress, arc plasma shear stress, and arc pressure are all transformed to the localized body forces and added to the momentum transport equations as source terms at the boundary cells.

2.5. Energy transfer at the arc plasma and metal interface

At the plasma–electrode interface, there exists an anode sheath region [25]. In this region, the mixture of plasma and metal vapor departs from LTE, thus it no longer complies with the model presented above. The thickness of this region is about 0.02 mm [25]. Since the sheath region is very thin, it is treated as a special interface to take into account the thermal effects on the electrode. The energy balance equation at the surface of the anode is modified to include an additional source term, S_a, as the following [8,9] for the metal region

$$S_a = \frac{k_{eff}(T_{arc} - T_a)}{\delta} + J_a\phi_w - \varepsilon k_bT_a^4 - q_{ev}H_{ev}. \tag{18}$$

The first term on the right-hand side of Eq. (18) is the contribution due to thermal conduction from the plasma to the anode. The symbol k_{eff} represents the thermal conductivity taken as the harmonic mean of the thermal conductivities of the arc plasma and the anode material. δ is the length of the anode sheath region and the maximum experimentally observed thickness of the anode fall region is 0.1 mm [35]. T_{arc} is chosen to be the temperature of the first gas plasma cell along the normal direction, and T_a is the temperature of the first metal cell along the normal direction at the local point. The second term represents the electron heating associated with the work function of the anode material. J_a is the square root of J_r^2 and J_z^2 and ϕ_w is the work function of the anode material. The third term is the black body radiation loss from the anode surface. The final term is the heat loss due to the evaporation of electrode materials. ε is the emissivity of the surface and k_b is the Stefan–Boltzmann constant. q_{ev} is the mass rate of evaporation of metal vapor from the droplet, and H_{ev} is the latent heat of vaporization. For metal, such as steel, q_{ev} can be written as [34]

$$\log(q_{ev}) = A_v + \log P_{atm} - 0.5 \log T, \tag{19}$$

$$\log P_{atm} = 6.121 - \frac{18836}{T}. \tag{20}$$

At the arc-anode interface, the energy equation for the plasma only considers the cooling effects through conduction and the source term, S_{ap}, is given

$$S_{ap} = -\frac{k_{eff}(T_{arc} - T_a)}{\delta}. \tag{21}$$

Similar to the anode region, there exists a cathode sheath region between the plasma and the cathode. However, the physics of the cathode sheath and the energy balance at the nonthermionic cathode for GMAW are not well understood [8–12,27]. The thermal effect due to the cathode sheath has been omitted in many models and reasonable results were obtained [8–12]. Thus, the energy balance equation at the cathode surface will only have the conduction, radiation, and evaporation terms

$$S_c = \frac{k_{eff}(T_{arc} - T_c)}{\delta} - q_{ev}H_{ev} - \varepsilon k_b T_c^4, \tag{22}$$

where k_{eff} is the effective thermal conductivity at the arc-cathode surface taken as the harmonic mean of the thermal conductivities of the arc plasma and the cathode material. δ is the length of the cathode sheath region. T_c is the cathode surface temperature. The heat loss from the plasma at the cathode surface is

$$S_{cp} = -\frac{k_{eff}(T_{arc} - T_c)}{\delta}. \tag{23}$$

2.6. Boundary conditions

The boundary conditions for solution of Eqs. (1)-(7) are given as follows.

2.6.1. External boundary conditions

The calculation domain, as shown in Fig. 1, is ABCDEFGA. Only half of the entire physical domain is calculated due to the cylindrical symmetry along the centerline AG. The corresponding external boundary conditions for the entire domain are listed in Table 1. Symmetrical boundary conditions are used along the centerline AG. The wire feed rate is incorporated through a boundary condition on v along AB. The imposed shielding gas flow is set through a boundary condition on v along BC. For the inflow of gas from the nozzle, the radial velocity component is omitted and the axial velocity component is determined from the formula for pipe flow as shown in the following [36]:

$$v(r) = \frac{2Q}{\pi} \frac{\left\{ R_n^2 - r^2 + \left(R_n^2 - R_w^2 \right) \frac{\ln(r/R_n)}{\ln(R_n/R_w)} \right\}}{\left\{ R_n^4 - R_w^4 + \frac{\left(R_n^2 - R_w^2 \right)^2}{\ln(R_n/R_w)} \right\}} + V_w \frac{\ln\frac{R_n}{r}}{\ln\frac{R_n}{R_w}}, \tag{24}$$

where Q is the inflow rate of the shielding gas, R_w is the radius of the electrode, R_n is the internal radius of the shielding gas nozzle, and V_w is the wire feed rate. A constant mass flow boundary condition is used for the open boundaries CD and DE.

Table 2
Thermophysical properties of mild steel and other parameters.

Nomenclature	Symbol	Value (unit)
Constant in Eq. (19)	A_v	2.52
Specific heat of solid phase	c_s	700 (J kg^{-1} K^{-1})
Specific heat of liquid phase	c_l	780 (J kg^{-1} K^{-1})
Thermal conductivity of solid phase	k_s	22 (W m^{-1} K^{-1})
Thermal conductivity of liquid phase	k_l	22 (W m^{-1} K^{-1})
Density of solid phase	ρ_s	7200 (kg m^{-3})
Density of liquid phase	ρ_l	7200 (kg m^{-3})
Thermal expansion coefficient	β_T	4.95×10^{-5} (K^{-1})
Radiation emissivity	ϵ	0.4
Dynamic viscosity	μ_l	0.006 (kg m^{-1} s^{-1})
Latent heat of fusion	H	2.47×10^5 (J kg^{-1})
Latent heat of vaporization	H_{ev}	7.34×10^6 (J kg^{-1})
Solidus temperature	T_s	1750 (K)
Liquidus temperature	T_l	1800 (K)
Ambient temperature	T_∞	300 (K)
Vaporization temperature	T_{ev}	3080 (K)
Surface tension coefficient	γ	1.2 (N m^{-1})
Surface tension temperature gradient	$\partial\gamma/\partial T$	10^{-4} (N m^{-1} K^{-1})
Work function	ϕ_w	4.3 (V)
Electrical conductivity	σ_e	7.7×10^5 (Ω^{-1} m^{-1})
Shielding gas flow rate	Q	24 (L min^{-1})
Internal diameter of shielding gas nozzle	d_n	19.1 (mm)
Electric power to weld	$u_w \cdot I$	3500 (W)
Electrode diameter	d	1.6 (mm)
Wire feed speed	V_w	4.5 (cm s^{-1})

The temperature boundaries along AD, DE, and EG are determined by the ambient condition, which is set as room temperature. Uniform current density is specified along AB as $J_z = -\sigma_e \frac{\partial\phi}{\partial z} = \frac{I}{\pi R_w^2}$. The voltage, ϕ, is set to zero at the bottom of the workpiece FG.

2.6.2. Internal boundary conditions

Within the computational domain, the moving surface of the electrode, droplet and weld pool forms the inner boundary for the arc region. VOF Eq. (12) is solved in the metal domain to track the moving free surface with free boundary conditions set at the metal free surface. Additional body force source terms are added to the momentum transport equations at the metal free surface to consider the effects of surface tension, Maragoni shear stress, arc plasma shear stress and arc pressure. Additional source terms described in Eqs. (18) and (22) are added to the energy equation for the special treatment of the anode sheath and the cathode sheath.

A fixed computational domain is used to solve the equations in the arc region. The metal region is used as the inner boundary for the arc region. As the velocity in the metal domain is much smaller than the velocity of the arc plasma, the metal region serves as an inner obstacle in the arc domain. The temperature at the metal free surface is considered as the temperature boundary for the arc domain. Additional source terms described in Eqs. (21) and (23) are added to the energy equation for the arc near the anode and cathode.

3. Numerical considerations

In the present study, the transport phenomena in the metal and the arc plasma are calculated separately in the corresponding

Table 1
Boundary conditions on the outer boundaries.

	AB	BC	CD	DE	EF	FG	GA
u	0	0	0	$\frac{\partial(\rho u)}{\partial r} = 0$	0	0	0
v	v_w	Eq. (24)	$\frac{\partial(\rho v)}{\partial z} = 0$	0	0	0	$\frac{\partial v}{\partial r} = 0$
h	$T = 300$ K	$T = 300$ K	$T = 300$ K	$T = 300$ K	$T = 300$ K	$T = 300$ K	$\frac{\partial T}{\partial r} = 0$
ϕ	$-\sigma\frac{\partial\phi}{\partial z} = \frac{I}{\pi R_c^2}$	$\frac{\partial\phi}{\partial z} = 0$	$\frac{\partial\phi}{\partial z} = 0$	$\frac{\partial\phi}{\partial r} = 0$	$\phi = 0$	$\phi = 0$	$\frac{\partial\phi}{\partial r} = 0$

metal domain and arc domain, and the two domains are coupled through the interfacial boundary conditions at each time step. The current continuity equation and its associated boundary conditions are solved for the entire domain, while other primary variables, including p, u, v, and T, are calculated separately in the metal domain and arc domain. The current continuity equation is iterated with the transport equations in the arc domain to obtain the current density distribution for both the arc domain and the metal domain. Iterations are required to assure convergence of each domain and then the boundary conditions are calculated from each domain for the coupling between the two domains.

For the metal domain, the method developed by Torrey et al. [31] was used to solve p, u, v, and T. This method is Eulerian and allows for an arbitrary number of segments of free surface with any reasonable shape. The basic procedure for advancing the solution through one time step, Δt, consists of three steps. First, at the beginning of each time step, explicit approximations to the momentum Eqs. (2) and (3) are used to find provisional values of the new time velocities. Second, an iterative procedure is used to solve for the advanced time pressure and velocity fields that satisfy Eq. (1) to within a convergence criterion at the new time. Third, the energy equation is solved.

For the arc plasma domain, a fully implicit formulation is used for the time-dependent terms, and the combined convection/diffusion coefficients are evaluated using an upwind scheme. The SIMPLE algorithm [37] is applied to solve the momentum and mass continuity equations to obtain the velocity field. At each time step, the current continuity equation is solved first, based on the updated parameters. The new distributions of current density and electromagnetic force are then calculated for the momentum and energy equations. The momentum equations and the mass continuity equation are then solved in the iteration process to obtain pressure and velocity. The energy equation is solved to get the new temperature distribution. Next, the temperature-dependent parameters are updated, and the program goes back to the first step to calculate the current continuity equation. This process is repeated for each time step until the convergence criteria are satisfied.

The governing differential equations (Eqs. (1)–(5) and Eq. (12)) and all related supplemental and boundary conditions are solved through the following iterative scheme:

1. At $t = 0$, the electrode is set up at an initial position and initial temperature distribution is given to the metal domain. Based on the initial fixed metal domain and temperature distribution,
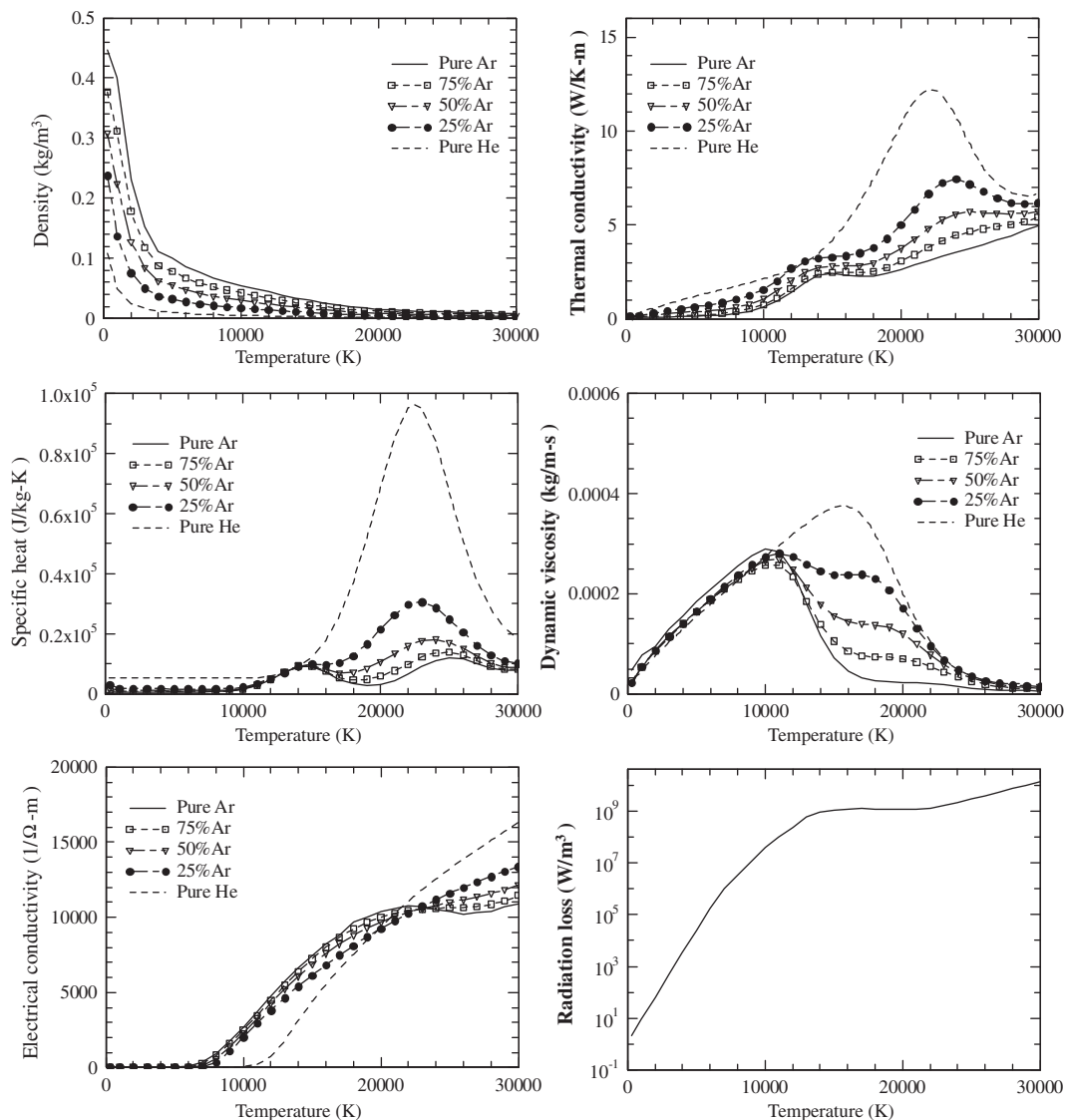

Fig. 2. The temperature-dependant material properties of shielding gases and the volume radiation heat loss taken from [27,38–40].

the initial distributions of temperature, velocity, pressure and current are obtained by solving the steady state equations in the arc domain (this procedure is similar to the steps from 5 to 7 for the steady state).

2. Surface tension, Marangoni shear stress, electromagnetic force, plasma shear stress and arc pressure are calculated, and other associated boundary conditions are evaluated for the metal domain.

3. Eqs. (1)–(4) are solved iteratively to obtain pressure, velocity and temperature in the metal domain.

4. Eq. (12) is solved to obtain the new free surface profile for the metal domain. The physical properties in the mesh cells and the boundary conditions within the computing domain are updated.

5. The current continuity Eq. (5) is solved in the whole domain with updated parameters. Current density and electromagnetic force are calculated.

6. Eqs. (1)–(3) and the associated boundary conditions are solved iteratively to get the velocity and pressure distributions of the arc plasma. When solving these equations, the electrode, droplet and the workpiece are treated as fixed inner obstacles.

7. Energy Eq. (4) is solved in the arc domain to get the new temperature distribution. Thermal physical properties of the arc plasma are updated. From here, the iteration goes back to step 5 to repeat the process for new distribution of current density, velocity, pressure, and temperature, until convergence criteria are satisfied.

8. Advance to the next time step and back to step 2 until the desired time is reached.

A FORTRAN program was compiled to implement the above algorithm. The calculation domain is half of the cylinder of 5.0 cm in radius and 3.05 cm in length. Extensive tests using different grid sizes and time step sizes have been conducted to assure
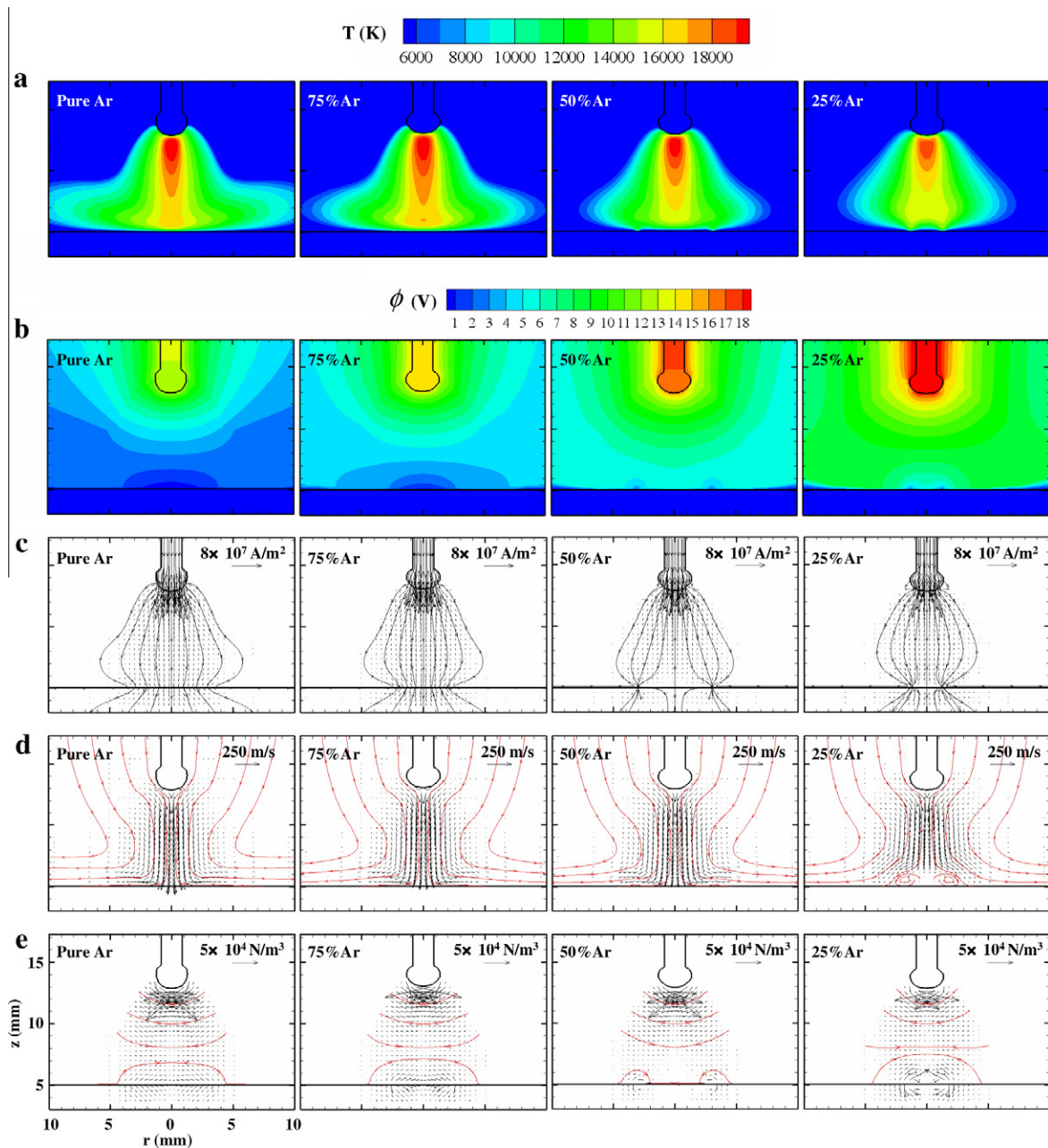

Fig. 3. The distributions of (a) temperature, (b) electrical potential, (c) current, (d) velocity and (e) electromagnetic force at $t = 90$ ms for pure Ar, 75% Ar, 50% Ar and 25% Ar.

consistent results. The final grid and time-step sizes used in the present study can be considered as the compromised values between computational time and accuracy. A non-uniform grid point system is employed with finer grid sizes near both the cathode and the anode. The mesh sizes near the anode and cathode center are set as 0.01 cm. The time step size is set as 5×10^{-6} s.

4. Results and discussion

4.1. Welding condition and the shielding gas properties

In this section, the results are presented for arcs operating in pure argon and argon–helium mixtures with various molar argon contents (75% Ar, 50% Ar and 25% Ar). Generally, welding conditions employed for various shielding gases are quite different, including the current, arc length, wire feed speed, gas flow rate and so on [1]. However, the intent of this study is to compare the effects of different shielding gases on arc characteristics and, hence, for comparison purpose, in this study the electric power input ($u_w \times I = 3500$ W), arc length, wire feed speed, etc., are assumed to be the same for various shielding gases. A 1.6-mm-diameter mild steel wire is fed continuously towards the workpiece at a wire feed speed of 4.5 cm/s. The initial arc length is set as 0.8 cm. The workpiece is also a mild steel disk with a 3 cm diameter and 0.5 cm thickness. The shielding gas flows out of the gas nozzle with a 1.91 cm inner diameter at a rate of 24 L/min. The thermophysical properties of mild steel and the other parameters used in the calculation are summarized in Table 2.

The temperature-dependant thermophysical properties of pure argon [27,38], pure helium and argon–helium mixtures at equilibrium [38–40], and the volume radiation heat loss (S_R) [27] are drawn in Fig. 2. It is seen that when temperatures are below about 750 K the electrical conductivities are nearly zero for all gases. As temperature increases, argon starts to be ionized, which results in higher electrical conductivities for higher argon contents until about 22,000 K. At this high temperature helium starts to be ionized and the electrical conductivities increase with helium content due to the more effective ionization of helium. The thermal conductivity and specific heat of helium are higher than those of argon, especially at temperatures above 15,000 K. Hence, a higher helium content of shielding gas leads to a higher thermal conductivity and specific heat. The viscosities of argon–helium mixtures remain approximately the same at lower temperatures, but at temperatures above 12,000 K mixtures with higher helium content have much higher viscosities. Due to the lack of radiation loss for pure helium and argon–helium mixtures, the data of argon [27] is used for all cases, which should not lead to significant errors [18]. Note the presence of metal vapor increases the electrical conductivity in helium-rich arc and contributes to arc stability [18], which is, however, ignored in this study.

In practice, a touch striking or a pilot starting arc is needed to initiate the main electric arc for welding. In this study, an initial high temperature ($T = 25,000$ K) arc column is assumed for arc initiation, which can be sustained by itself and reaches the working status after several numerical iterations for all cases. The time is set as $t = 0$ s when the arc is established in all cases. However, the calculation using the physical properties for pure helium is diverged because the electrical conductivity for pure helium is so small at temperatures less than 9000 K (Fig. 2) that an arc cannot sustain itself. In fact, in practice, pure helium has seldom been used as shielding gas because of arc instability. Hence, we do not consider pure helium in this study. In all the following figures, the shapes of the electrode and workpiece are marked with thick solid lines. In order to increase the readability of vectors, only a quarter

of the grid nodes are used for plotting the distributions of velocity, current and electromagnetic force.

4.2. Arc parameters in different shielding gases

Fig. 3(a)–(e), respectively, show the distributions of temperature, electrical potential, current, velocity streamline and electromagnetic force at $t = 90$ ms. From Fig. 3(a), it is seen the outer shape of the temperature profile between the electrode tip and the workpiece for each case (pure Ar, 75% Ar, 50% Ar and 25% Ar) looks like a "bag" closed at the top. In the argon-rich cases (pure Ar or 75% Ar), a typical bell-shaped plasma arc is found. The arc expands outward and downward, resulting in the decrease of its temperature toward the workpiece surface. As the helium content increases, the arc tends to contract in the lower part of the arc column and forms a cone-like shape. Near the electrode tip, the shielding gas begins to ionize and forms a high temperature arc column underneath the tip. At a constant electric power, the arc peak temperature occurring on the axis near the electrode tip decreases with the increasing helium content and it is, respectively, 20,240 K, 20,130 K, 20,100 K and 18,870 K for pure Ar, 75% Ar, 50% Ar and 25% Ar. In comparison with pure argon, the addition of a small amount of helium to argon (e.g., 75% Ar) produces a slightly larger hot arc column. However, the size of the hot arc column significantly decreases in the case of 25% Ar. This is attributed to the high ionization potential of helium. For 25% Ar, as there is a large amount of helium in the mixture, the ionization degree of the mixture sharply decreases, which leads to a drop in arc temperatures. Due to less ionization, the lower part of the arc column is
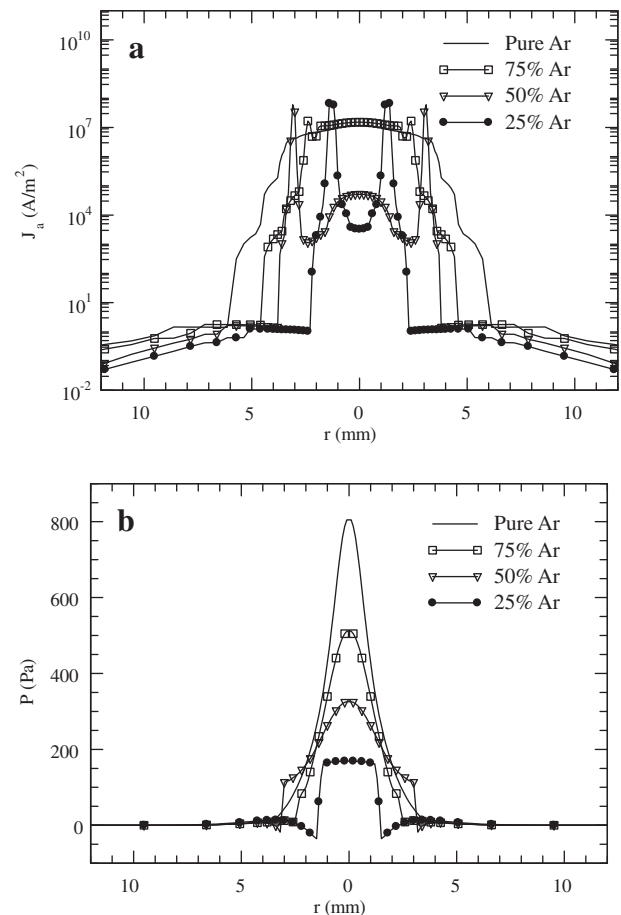

Fig. 4. The current density and arc pressure distributions along the workpiece surface at $t = 90$ ms: (a) current density and (b) arc pressure.

at low temperatures, resulting in a shrinkage of the size of the hot arc column for high helium contents (50% and 25% Ar).

As shown in Fig. 3(b), the larger electrical potential contours are found in high helium cases, and the maximum electrical potentials located at the end of contact tube are, respectively, 15.22 V, 16.67 V, 18.92 V, and 21.60 V for pure Ar, 75% Ar, 50% Ar and 25% Ar at t = 90 ms. Due to the higher ionization potential of helium, a higher voltage is required to establish and maintain the stability of the plasma arc as helium content increases. The sharply varied voltage drops in the arc near the workpiece are observed, especially for high helium contents. Note a cathode sheath exists between the plasma and the cathode. The sheath voltage is related to electron emission at the cathode, and the physics involved are extremely complex and not well understood [8–12]. In this model, the electrode sheath is treated as the special boundary to take into account the thermal effects on the plasma. Due to the cooling effect (Eq. (23)), the plasma very close to the workpiece has quite low temperatures, which in turn decreases the electrical conductivity, especially for high helium contents (see Fig. 2). As a result, the larger arc voltage drop is created (Eq. (6)).

At a constant electric power, the welding current is inversely proportional to the arc voltage and, therefore, decreases with the increase of helium content. During the GMA welding process, the welding current fluctuates, as the voltage does, in a narrow range. The currents at t = 90 ms are, respectively, about 230 Å, 210 Å, 185 Å and 162 Å for pure Ar, 75% Ar, 50% Ar and 25% Ar. As shown in Fig. 3(c), current generally diverges downward from the electrode tip, then converges at the surface of the workpiece, and finally diverges inside the workpiece. For argon-rich cases, the current converges to the surface of the workpiece at a larger "disk" area; while as the helium content increases, the current converges to a "ring" or "circle" (from an axisymmetric standpoint) surrounding the center of the workpiece. As the plasma temperature is caused by Joule heating, Eq. (4), the temperature distribution of the plasma arc, shown in Fig. 3(a), is proportional to the magnitude and distribution of the current, Fig. 3(c).

As shown in Fig. 3(d), the shielding gas from the nozzle flows along the electrode surface and is ionized to become plasma around the electrode tip. Due to the action of the inward and downward electromagnetic force around the electrode tip,
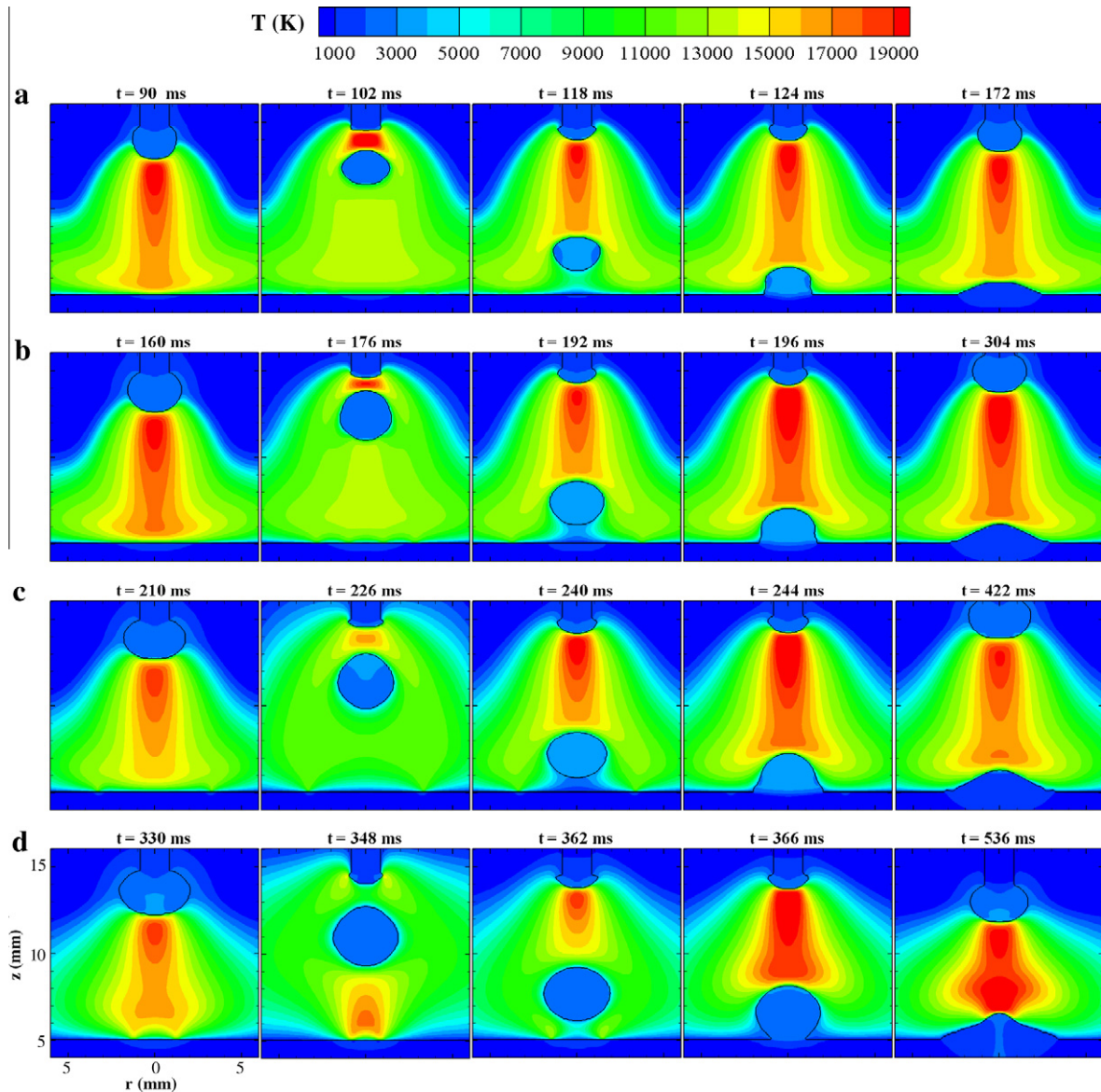

Fig. 5. The sequence of temperature distribution in plasma arcs at different instants: (a) pure Ar, (b) 75% Ar, (c) 50% Ar and (d) 25% Ar.

Fig. 3(e), the plasma is accelerated and flows inward and downward toward the workpiece with very high velocities. The maximum velocities are, respectively, 269, 254, 253 and 210 m/s for pure Ar, 75% Ar, 50% Ar and 25% Ar. However, near the workpiece, the electromagnetic force becomes inward and upward, Fig. 3(e), which gives an opposite action on the plasma flow along the z-axis. For argon-rich cases, the upward electrometric force near the workpiece is not too strong and, hence, the downward arc plasma impinges onto the workpiece and thereafter flows outward due to the stagnation effect. As the helium content increases, the upward electromagnetic force near the workpiece increases. For 25% Ar case, the downward plasma flow is counteracted by the upward electromagnetic force near the workpiece and is greatly decelerated, generating vortexes near the workpiece center. Similar phenomena for He −10% Fe arc were also predicted by Jönsson et al. [18]. The outward vortex near the center of the workpiece surface prevents the hot plasma from being transported from the electrode to the workpiece for high helium arc. The vortex also brings in the colder gas from outside of the arc column to the center, which further decreases the arc temperature near the workpiece.

The variations of current density and arc pressure along the radial direction from the z-axis on the workpiece surface at $t = 90$ ms are shown in Fig. 4(a) and (b), respectively. It is seen that the radius of the "disk" with high current density signifi-cantly decreases from about $r = 6$ mm for pure Ar to a little greater than 2 mm for 25% Ar, which is consistent with the results shown in Fig. 3(c). For all cases, there exists an abrupt decrease of current density in the radial direction and thereafter the current density becomes negligible. For argon-rich cases, the current density is fairly smooth and uniform near the center $r = 0$ with its peak at the center. For 50% Ar and 25% Ar cases, however, the current density curve fluctuates significantly and there are two peaks (which actually is a "ring" or "circle" because of an axisymmetric coordinate system). These peaks coincide with the converged "ring" as shown in Fig. 3(c). From Fig. 4(b), the arc pressure generally has a Gaussian-like distribution, except for the 25% Ar case, in which a rather uniform flat-top pressure exists near the center. The peak of the arc pressure decreases significantly as the helium content increases. The arc pressure decreases to nearly zero at about $r = 3$ mm. The high pressure near the center is caused by the stagnation effect when the plasma flow impinges onto the workpiece. As the argon content decreases, the arc pressure becomes smaller in both magnitude and scope. This is caused by the significant decrease of the downward plasma velocity near the workpiece, resulting in the decrease of arc pressure as explained in Fig. 3(d). It is seen in Fig. 4(b) negative pressures less than the ambient pressure are created at the edge of the "ring" for helium-rich shielding gases.
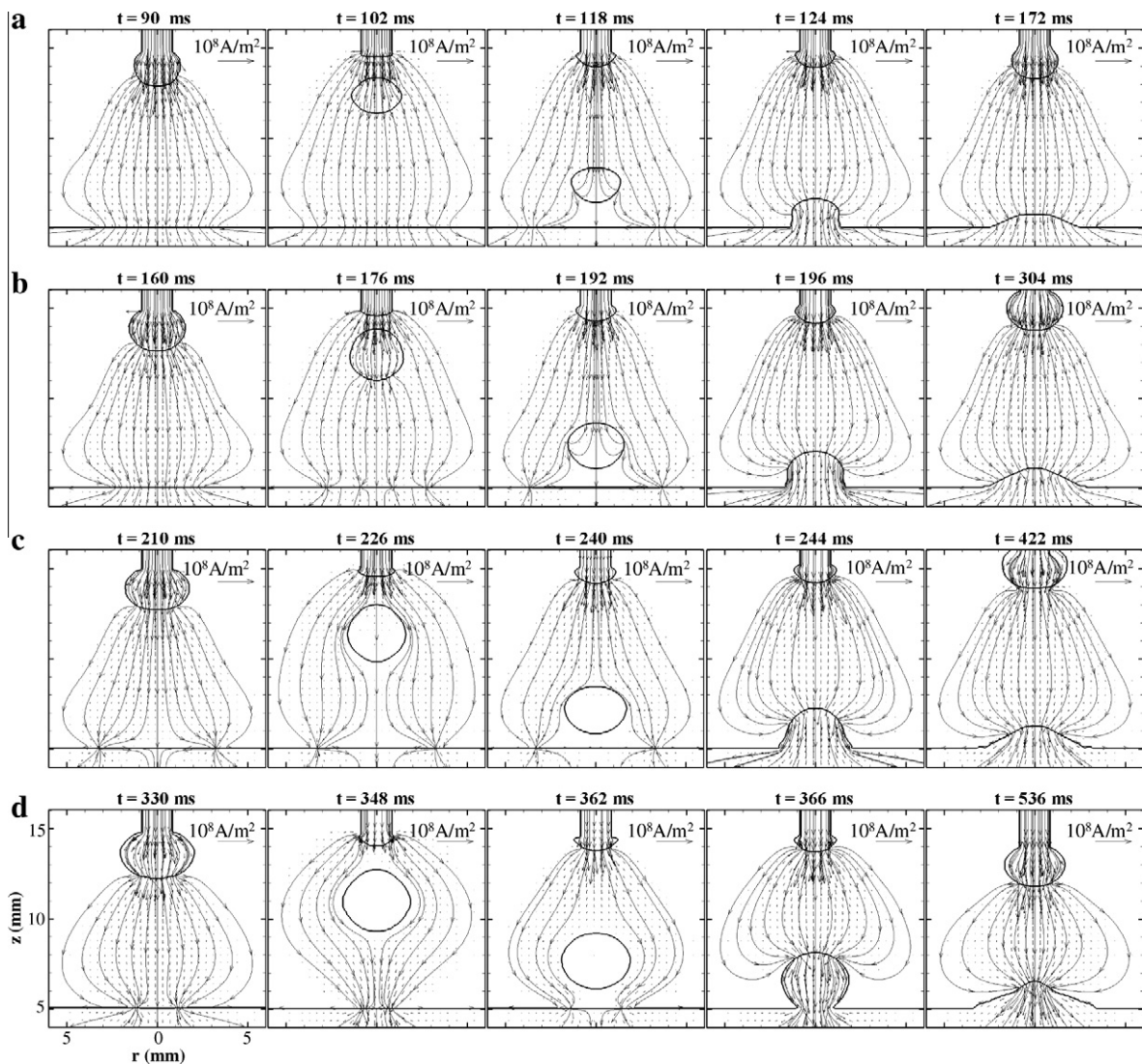

Fig. 6. The sequence of current distribution in plasma arcs at different instants: (a) pure Ar, (b) 75% Ar, (c) 50% Ar and (d) 25% Ar.

4.3. Arc evolution in different shielding gases

Figs. 5–8 show, respectively, the distributions of temperature, current density, velocity, and electromagnetic force in arc plasma at different instants for different argon–helium mixtures. The transient processes of droplet formation, detachment, transfer and impingement onto the workpiece and how they affect the transport phenomena of the plasma arcs are shown in these figures. Note in order to better explain the transport phenomena, the selected instants for each subfigure are different for each case, and the time intervals between two subfigures in each case are not equal either. From the figures, it is seen the times for the formation of the first droplet are longer for higher helium contents, and the times are, respectively, about 100 ms, 170 ms, 217 ms and 336 ms for pure Ar, 75% Ar, 50% Ar and 25% Ar. The addition of helium results in a lower detachment frequency and thus a larger droplet for the same welding energy input. This is consistent with the phenomena observed by Rhee and Kannatey-Asibu [41] that the droplet frequency using pure argon is much higher than that for helium. In all cases the falling droplet greatly alters and distorts the arc flow and arc characteristics. In the following, as the distribution of arc plasma temperature is influenced by current density, for convenience, Figs. 5 and 6 are discussed alternatively. Similarly,

as the distribution of plasma velocity is influenced by electrometric force, Figs. 7 and 8 will be discussed together.

As shown in Fig. 5, before the detachment of the droplet, an arc column with high temperatures exists between the electrode tip and the top surface of the workpiece. The structure and shape of the arc column are different with different argon contents. When the droplet is detached from the electrode, a new arc column is formed between the electrode tip and the top surface of the detached droplet. As the detached droplet falls, the plasma arc column is "stretched" between the electrode tip and the top of the falling droplet. Due to the lower ionization potential of argon, it is easier and quicker for argon-rich shielding gas to re-establish a new arc column after the droplet detachment. It is seen a new arc column with high temperatures has been established at $t = 102$ ms for pure argon, while at $t = 348$ ms, there is a weak arc column between the electrode tip and the droplet for 25% Ar. The falling droplet blocks the plasma arc and the arc temperature below the droplet is relatively low. However, it is interesting to see in Fig. 5(d) at $t = 348$ ms, there exists a hot arc column between the bottom of the droplet and the workpiece for 25% Ar. This is caused by the strong current convergence at the workpiece, Fig. 6(d), which results in a high Joule heating. After the first droplet deposits onto the workpiece and the second droplet grows at the tip of
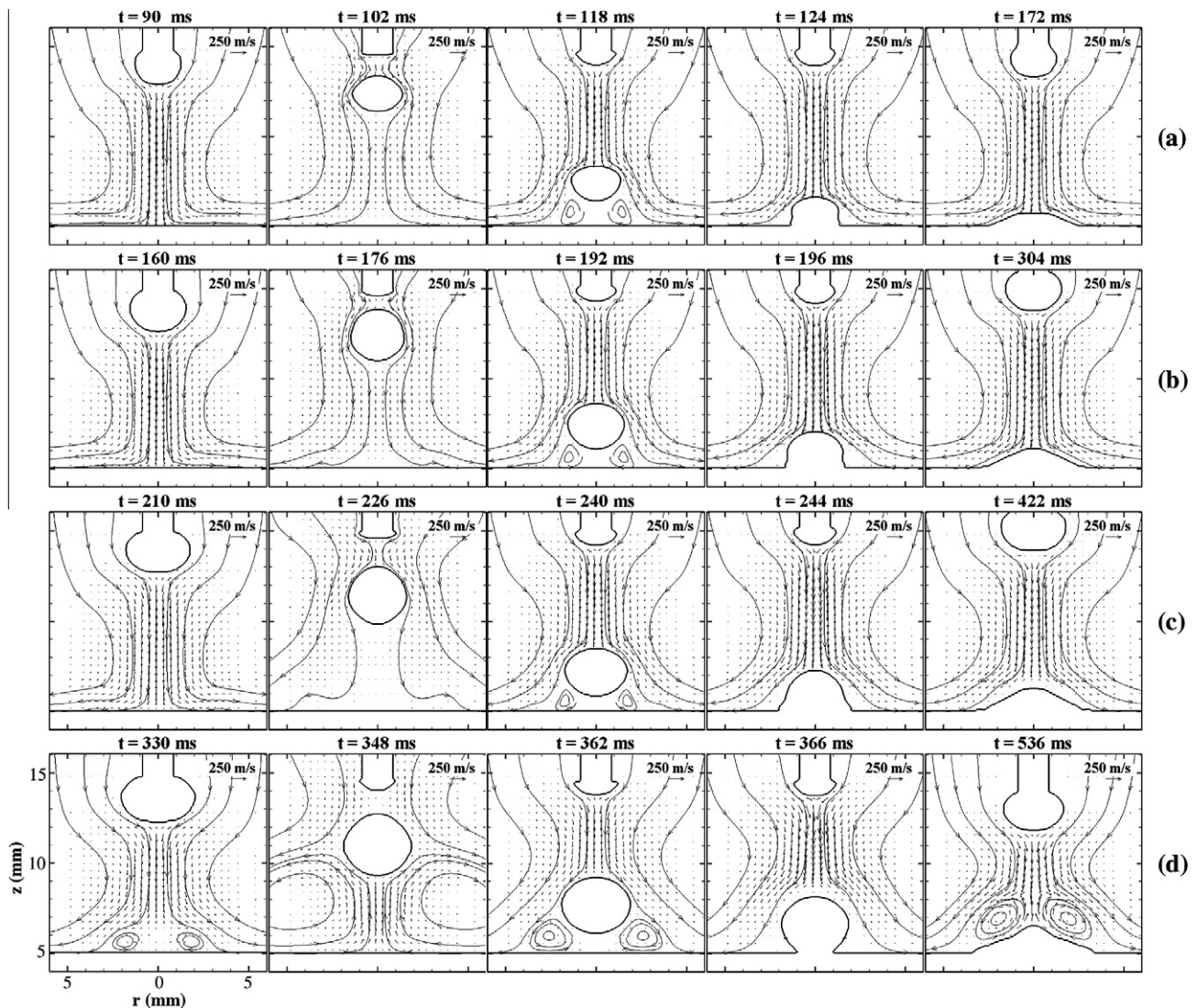

Fig. 7. The sequence of velocity distribution in plasma arcs at different instants: (a) pure Ar, (b) 75% Ar, (c) 50% Ar and (d) 25% Ar.

the electrode, Fig. 5(d), at t = 536 ms, the distance between the electrode tip and the workpiece is short, which results in "double hot spots;" one is beneath the electrode and the other is above the workpiece. The plasma arc column looks like it is being "squeezed" and "bulged". The lower hot spot is caused by the strong current convergence, Fig. 6(d), similar to the result at t = 348 ms.

Fig. 6 shows the current distributions at different instants for different shielding gases. For argon-rich cases, Fig. 6(a) and (b), when the droplet has just been detached, the current can flow through the detached droplet because of high electrical conductivity and high current density of the plasma surrounding the droplet. However, less current flows through and part of the current flows around the falling droplet, as it is further away from the electrode tip. Note as the arc plasma expands downward, its temperature, electrical conductivity, and current density decrease. The phenomenon of current flowing around the droplet can be better seen when the helium content increases. As helium content increases, the electrical conductivity of the shielding gas decreases, Fig. 2, which is compounded by the lower temperature underneath the falling droplet resulting in less current flowing through the detached droplet. As shown for 25% Ar case, there is almost no current flowing through the detached droplet. After bypassing around the detached droplet, the current arriving at the surface

of the workpiece tends to converge to an "annular" shape (e.g., Fig. 6(b) at t = 192 ms) instead of a "disk" shape (e.g., Fig. 6(a) at t = 90 ms) from an axisymmetric standpoint. As the helium content increases, the aforementioned current convergence at the workpiece becomes more severe. When the detached droplet is impinged onto the workpiece, a weld pool is formed and its shape determines the current flow into the workpiece.

Fig. 7 shows the arc plasma flows at different instants for different gas mixtures. Generally, for an argon-rich gas, the plasma flows downward around the droplet, impinges onto the workpiece, and then spreads outward along the workpiece due to the stagnation effect. When the falling droplet is close to the workpiece, e.g., Fig. 7(a) at t = 118 ms, two vortexes (in the r–z plane) are formed near the workpiece. In fact, for the 25% Ar case, at t = 330 ms, Fig. 7(d), two vortexes near the workpiece can be clearly seen even as the droplet is still being formed at the electrode tip. This is caused by a strong upward and inward electromagnetic force near the workpiece, Fig. 8(d). At t = 348 ms, the downward flow collides with the upward flow near the droplet and the two vortexes become larger when the droplet is in between the electrode tip and the workpiece because of a stronger electromagnetic force, Fig. 8(d). At t = 362 ms, however, the vortexes are "squeezed" by the falling droplet and become smaller as the electromagnetic force decreases. In Fig. 7(d), at t = 536 ms, two large vortexes
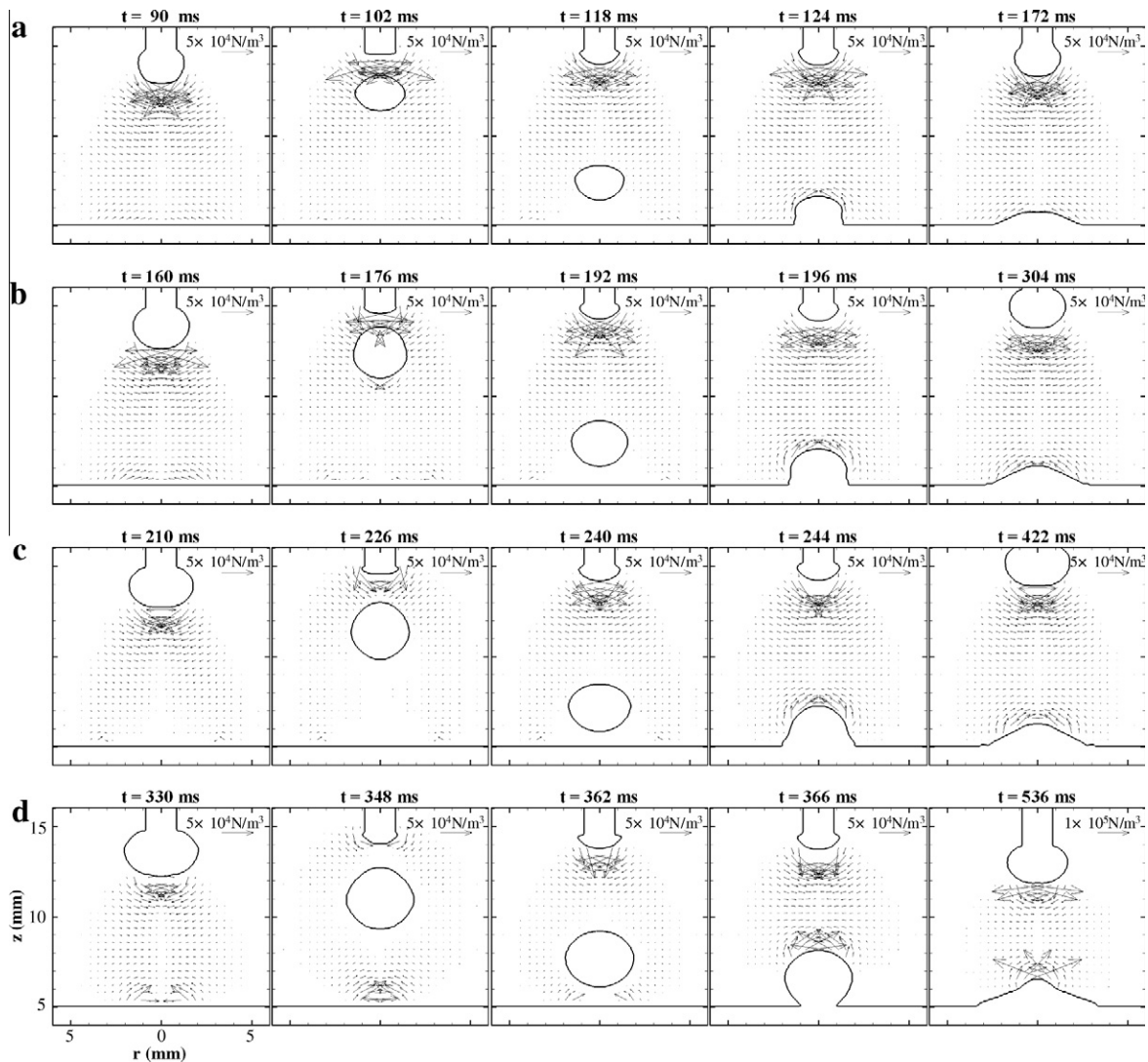

Fig. 8. The sequence of electromagnetic force distribution in plasma arcs at different instants: (a) pure Ar, (b) 75% Ar, (c) 50% Ar and (d) 25% Ar.

appear again near the workpiece, caused by the strong electromagnetic force, Fig. 8(d).

As shown in Fig. 8, generally, the electromagnetic force is inward and downward around the tip of the electrode, and inward and upward near the workpiece center. The downward plasma flow from the electrode counteracts with the upward flow from the workpiece, which may lead to the formation of vortexes. With the increase of helium content, the upward electromagnetic force from the workpiece becomes stronger, leading to a stronger upward arc flow. For the same welding energy input, as considered in this study, it is easier for argon-rich shielding gas to transport the hot plasma from the electrode to the workpiece. In other words, the welding efficiency would be higher when using argon-rich gases.

The arc pressure distribution also varies during the process of droplet formation, transfer and impingement, Fig. 9. Before the droplet detachment, there are two high-pressure regions; one is underneath the droplet and the other is above the workpiece, as shown in the first column of Fig. 9. The high pressure underneath the droplet is caused by the pinch effect of the electromagnetic force, which decreases with the increase of helium content at the

same energy input. The pressure near the workpiece also decreases as helium content increases, as discussed in Fig. 4(b). After the droplet is detached, a new arc pressure with two high-pressure regions forms between the electrode tip and the upper surface of the falling droplet, as shown in the third column of Fig. 9. The arc pressure underneath the falling droplet decreases due to the smaller plasma flow. After the droplet is impinged onto the workpiece, the arc pressure distribution resumes to the results similar to that in the first column, as shown in the fifth column of Fig. 9.

To further study the variation of arc pressure, the distributions of arc pressure along the workpiece surface at different instants corresponding to Fig. 9 are plotted in Fig. 10. Note the arc pressure distributions along the workpiece surface for the first column in Fig. 9 are similar to those in Fig. 4(b), although the subfigures in the first column of Fig. 9 are at different times. As compared to Fig. 4(b), after the droplet is detached and moves downward, the magnitudes of arc pressure decrease significantly but spread to a wider range, Fig. 10(a). Note the subfigures in the second column of Fig. 9 and the corresponding arc pressure distributions along the workpiece surface in Fig. 10(a) are at different times and the size and location of the droplet are different and, hence, the
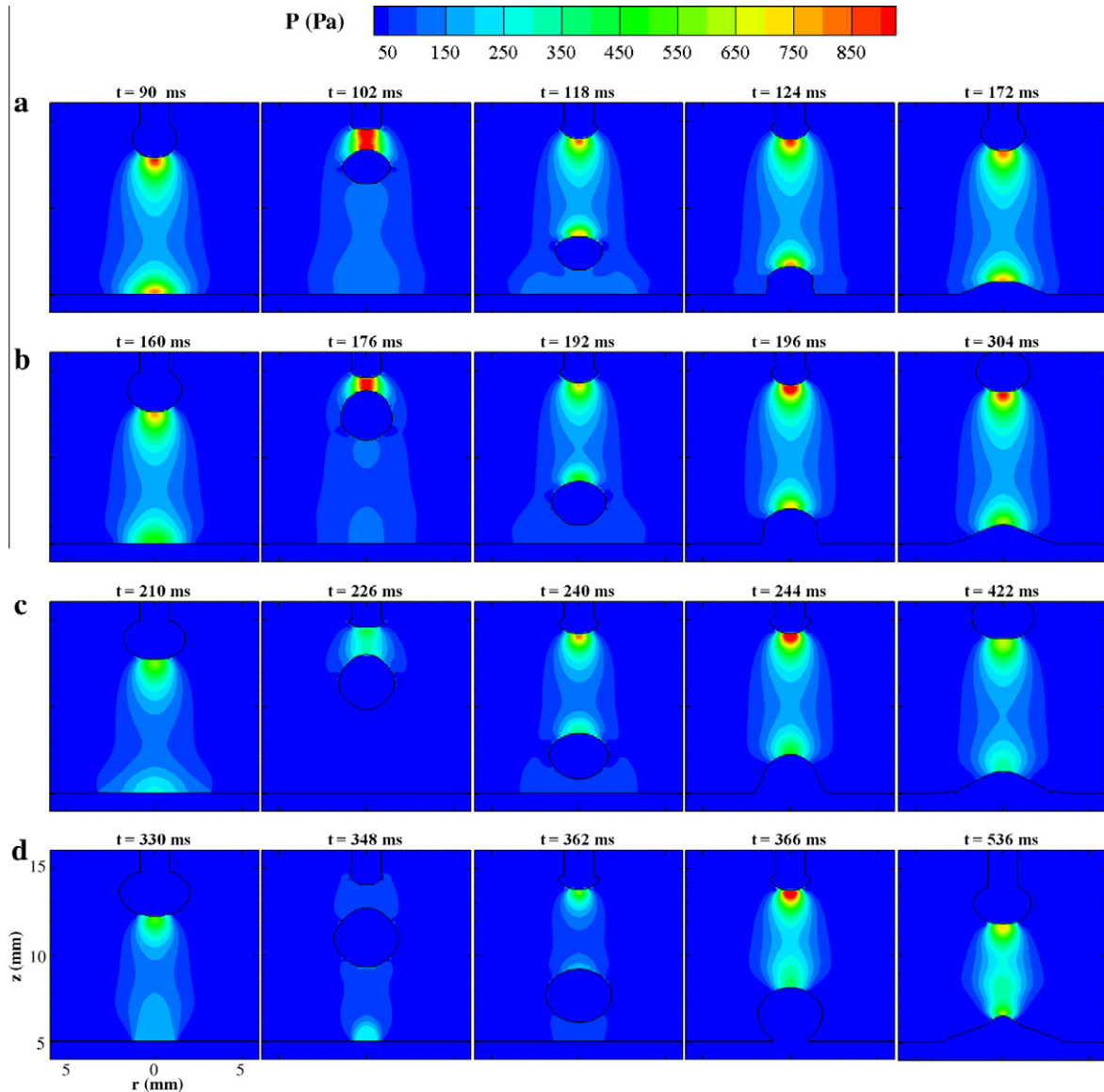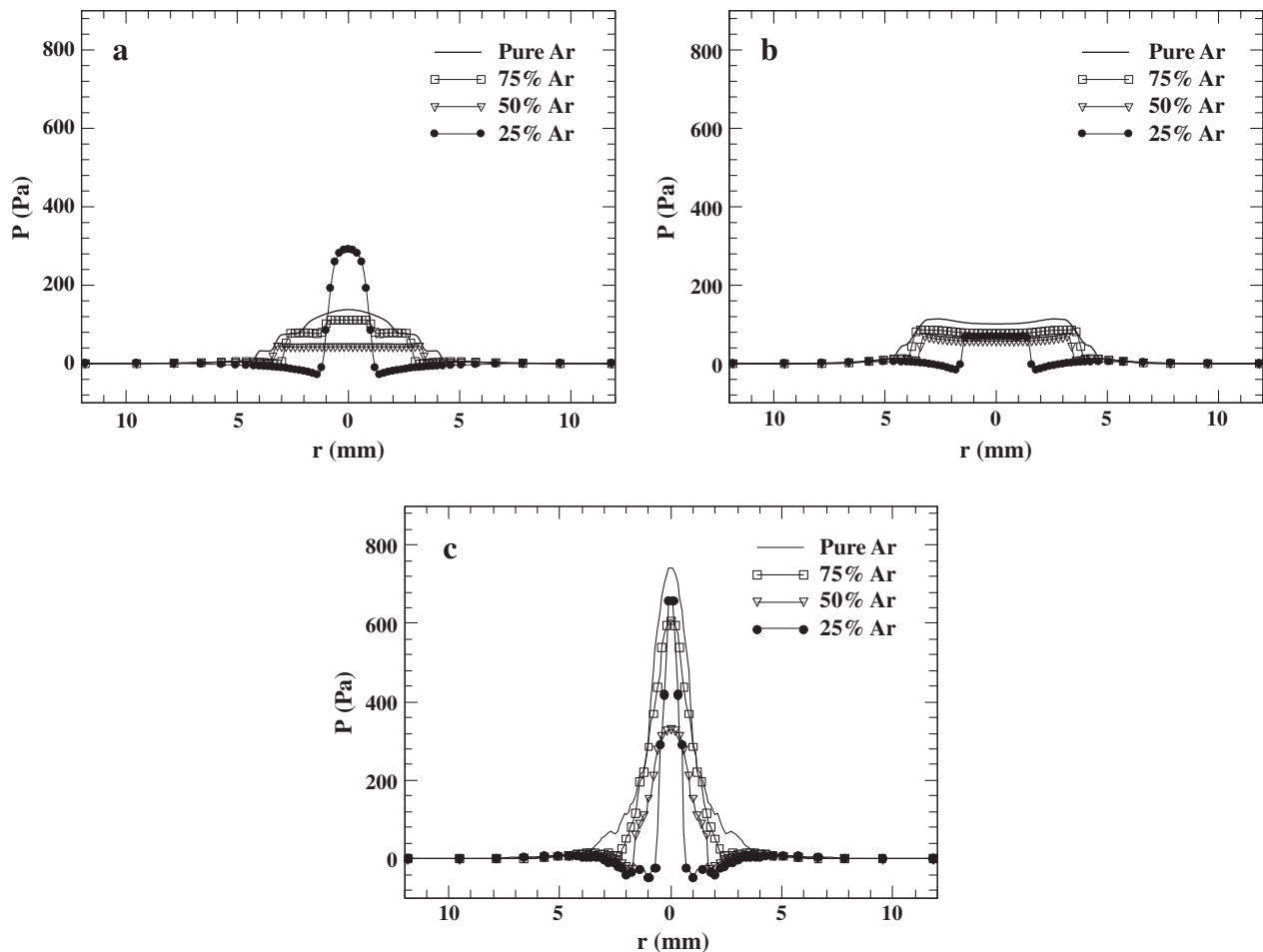

Fig. 9. The sequence of arc pressure distribution at different instants: (a) pure Ar, (b) 75% Ar, (c) 50% Ar and (d) 25% Ar.

Fig. 10. The arc pressure distribution along the workpiece surface at the different instants shown in Fig. 9: (a) the second column, (b) the third column and (c) the fifth column.

comparison here is only for the purpose of discussion of the general phenomena. As the droplet is very close to the workpiece, Fig. 10(b), the arc pressure distributions along the workpiece surface are nearly flat with very low magnitudes. After the droplet impinges onto the workpiece and becomes a weld bead, Fig. 10(c), the arc pressure distributions along the workpiece are similar to those before the droplet detachment (shown in Fig. 4(b)) except for the case of 25% Ar. Due to the strong arc contraction and current convergence for 25% Ar, the pressure near the center is larger in magnitude but narrower in scope compared to that before the droplet detachment, Fig. 4(b).

5. Conclusions

A comprehensive model has been applied to study the effects of shielding gas compositions on the transient transport phenomena occurring in GMAW. The generation and evolution; the droplet formation, detachment, transfer, and impingement onto the workpiece; and welding pool dynamics are studied for pure argon, 75% Ar + 25% He, 50% Ar + 50% He and 25% Ar + 75% He during the GMAW process. Compared to helium, argon has relatively lower ionization potential, thermal conductivity, specific heat, and viscosity, but higher electrical conductivity. From the results of this study, it is found that the thermophysical properties of shielding gases have pronounced effects on arc structure and characteristics. It is easy for argon to establish a stable plasma arc between the electrode tip and the workpiece. An increase of helium content

may lead to insufficient ionization of gas and, hence, a shrinkage of hot plasma arc. When helium increases to an extent, there is a strong upward plasma flow from the workpiece, leading to the distortions of temperature, velocity, pressure and current distributions. The higher helium content in the mixture leads to the higher degree of arc contraction, longer time to generate a droplet and thus larger droplet size. The plasma arc shape changes from a bell shape to a cone shape as the helium content increases. In conclusion, the shielding gas composition plays a vital role in plasma arc and, hence, the efficiency and overall performance of the GMA welding process.

References

[1] K.A. Lyttle, Shielding gas for welding, in: D.L. Olson, T.A. Siewert, S. Liu, G.R. Edwards (Eds.), ASM Handbook, Vol. 6: Welding, Brazing, and Soldering, American Society for Metals, Metal Park, OH, 1993, pp. 64–69.
[2] D.N. Shackleton, W. Lucas, Shielding gas mixtures for high quality mechanized GMA welding of Q&T steels, Weld. J. 53 (1974) 537s–547s.
[3] V.R. Dillenbeck, L. Catagno, The effects of various shielding gases and associated mixtures in GMA welding of mild steel, Weld. J. 66 (1987) 45–49.
[4] D.E. Hilton, J. Norrish, Shielding gases for arc welding, Weld. Met. Fabr. 56 (1988) 189–196.
[5] N. Stenbacka, K.A. Persson, Shielding gases for gas metal arc welding, Weld. J. 68 (1989) 41–47.
[6] N.E. Larson, W.F. Meredith, Shielding Gas Selection Manual, Union Carbide Industrial Gases Technology Corp., 1990.
[7] P. Zhu, M. Rados, S.W. Simpson, A theoretical study of gas metal arc welding system, Plasma Sources Sci. Technol. 4 (1995) 495–500.
[8] J. Haidar, A theoretical model for gas metal arc welding and gas tungsten arc welding. I, J. Appl. Phys. 84 (1998) 3518–3529.

[9] J. Haidar, J.J. Lowke, Predictions of metal droplet formation in arc welding, J. Appl. Phys. D: Appl. Phys. 29 (1996) 2951–2960.

[10] J. Haidar, An analysis of the formation of metal droplets in arc welding, J. Phys. D: Appl. Phys. 31 (1998) 1233–1244.

[11] J. Haidar, Prediction of metal droplet formation in gas metal arc welding II., J. Appl. Phys. 84 (1998) 3530–3540.

[12] J. Haidar, An analysis of heat transfer and fume production in gas metal arc welding. III, J. Appl. Phys. 85 (1999) 3448–3459.

[13] F.L. Zhu, H.L. Tsai, S.P. Marin, P.C. Wang, A comprehensive model on the transport phenomena during gas metal arc welding process, Prog. Comput. Fluid Dynam. 4 (2004) 99–117.

[14] H.G. Fan, R. Kovacevic, A unified model of transport phenomena in gas metal arc welding including electrode, arc plasma and molten pool, J. Phys. D: Appl. Phys. 37 (2004) 2531–2544.

[15] J. Hu, H.L. Tsai, Heat mass transfer in gas metal arc welding. Part I: The arc, Int. J. Heat Mass Transfer 50 (2007) 833–846.

[16] J. Hu, H.L. Tsai, Heat and mass transfer in gas metal arc welding. Part II: The metal, Int. J. Heat Mass Transfer 50 (2007) 808–820.

[17] J. Haidar, J.J. Lowke, Effect of CO_2 shielding gas on metal droplet formation in arc welding, IEEE Trans. Plasma Sci. 25 (1997) 931–936.

[18] P.G. Jönsson, T.W. Eagar, J. Szekely, Heat and metal transfer in gas metal arc welding using argon and helium, Metall. Trans. 26B (1995) 383–395.

[19] G.J. Dunn, T.W. Eagar, Metal vapors in gas tungsten arcs: Part II. Theoretical calculations of transport properties, Metall. Trans. 17A (1986) 1865–1871.

[20] A.B. Murphy, M. Tanaka, K. Yamamoto, S. Tashiro, T. Sato, J.J. Lowke, Modelling of thermal plasmas for arc welding: the role of the shielding gas properties and of metal vapour, J. Phys. D: Appl. Phys. 42 (2009) 194006.

[21] K. Yamamoto, M. Tanaka, S. Tashiro, K. Nakata, K. Yamazaki, E. Yamamoto, K. Suzuki, A.B. Murphy, Metal vapour behaviour in thermal plasma of gas tungsten arcs during welding, Sci. Technol. Weld. Join. 13 (2008) 566–572.

[22] J. Haidar, The dynamic effects of metal vapour in gas metal arc welding, J. Phys. D: Appl. Phys. 43 (2010) 165204.

[23] M. Schnick, U. Füssel, M. Hertel, A. Spille-Kohoff, A.B. Murphy, Metal vapour causes a central minimum in arc temperature in gas–metal arc welding through increased radiative emission, J. Phys. D: Appl. Phys. 43 (2010) 022001.

[24] J.J. Lowke, R. Morrow, J. Haidar, A simplified unified theory of arcs and their electrodes, J. Phys. D: Appl. Phys. 30 (1997) 2033–2042.

[25] J.J. Lowke, P. Kovitya, H.P. Schmidt, Theory of free-burning arc columns including the influence of the cathode, J. Phys. D: Appl. Phys. 25 (1992) 1600–1606.

[26] Q.Z. Diao, H.L. Tsai, Modeling of solute redistribution in the mushy zone during solidification of aluminum–copper alloys, Metall. Trans. 24A (1993) 963–973.

[27] J.F. Lancaster, The Physics of Welding, second ed., Oxford Pergamon, 1986.

[28] P.C. Carman, Fluid flow through granular beds, Trans. Inst. Chem. Eng. 15 (1937) 150–166.

[29] K. Kubo, R.D. Pehlke, Mathematical modeling of porosity formation in solidification, Metall. Trans. 16A (1985) 823–829.

[30] G.S. Beavers, E.M. Sparrow, Non-Darcy flow through fibrous porous media, J. Appl. Mech. 36 (1969) 711–714.

[31] M.D. Torrey, L.D. Cloutman, R.C. Mjolsness, C.W. Hirt, NASA-VOF2D: A computer program for incompressible flows with free surfaces, LA-10612-MS, Los Alamos National Laboratory, 1985.

[32] J.U. Brackbill, D.B. Kothe, C. Zemach, A continuum method for modeling surface tension, J. Comput. Phys. 100 (1992) 335–354.

[33] H.G. Fan, R. Kovacevic, Droplet, formation, detachment, and impingement on the molten pool in gas metal arc welding, Metall. Trans. 30B (1999) 791–801.

[34] T. Zacharia, S.A. David, J.M. Vitek, Effect of evaporation and temperature-dependent material properties on weld pool development, Metall. Trans. 22B (1992) 233–241.

[35] W. Finkelnburg, S.M. Segal, The potential field in around a gas discharge and its influence on the discharge mechanism, Phys. Rev. Lett. 83 (1951) 582–585.

[36] R.A. Granger, Fluid Mechanics, CBS College, New York, 1985. Chapter 10.

[37] S.V. Patanka, Numerical Heat Transfer and Fluid Flow, McGraw-Hill, New York, 1980.

[38] J. Aubreton, M.F. Elchinger, V. Rat, P. Fauchais, Two-temperature transport coefficients in argon–helium thermal plasmas, J. Phys. D: Appl. Phys. 37 (2004) 34–41.

[39] W.J. Lick, H.W. Emmons, Thermodynamic Properties of Helium to 50,000 K, Harvard University Press, Cambridge, MA, 1962. pp. 35–37.

[40] W.J. Lick, H.W. Emmons, Transport Properties of Helium from 200 to 50,000 K, Harvard University Press, Cambridge, MA, 1962. pp. 87–89.

[41] S. Rhee, E. Kannatey-asibu, Observation of metal transfer during gas metal arc welding, Weld. J. 71 (1992) 381s–386s.